In-silico experimentations of multimode shock response of polyurea

Carlos Gamez , Nha Uyen Huynh , George Youssef

PII: S0020-7403(21)00277-0
DOI: https://doi.org/10.1016/j.ijmecsci.2021.106542
Reference: MS 106542

To appear in: *International Journal of Mechanical Sciences*

Received date: 22 March 2021
Revised date: 17 May 2021
Accepted date: 18 May 2021

Please cite this article as: Carlos Gamez , Nha Uyen Huynh , George Youssef , In-silico experimentations of multimode shock response of polyurea, *International Journal of Mechanical Sciences* (2021), doi: https://doi.org/10.1016/j.ijmecsci.2021.106542

In-silico experimentations of multimode shock response of polyurea

Carlos Gamez, Nha Uyen Huynh, and George Youssef*

Experimental Mechanics Laboratory, Mechanical Engineering Department, San Diego State University, 5500 Campanile Drive, San Diego, Ca 92182-1323

Highlights

- The laser-induced waves generate accompanying waves at edges of loading site, e.g., induced pressure waves also generate shear and side spherical patterns pressure waves.
- The computational results demonstrate that the purity of loading type will depend on the geometrical configuration of the sample and delay of concurrent input waves.
- Depending on the targeted failure mechanism or stress state, in-silico experimentation of multimode shock waves can be done prior to or in tandem the physical experiment to determine parameters such as geometrical dimensions and loading type.

Graphical abstract

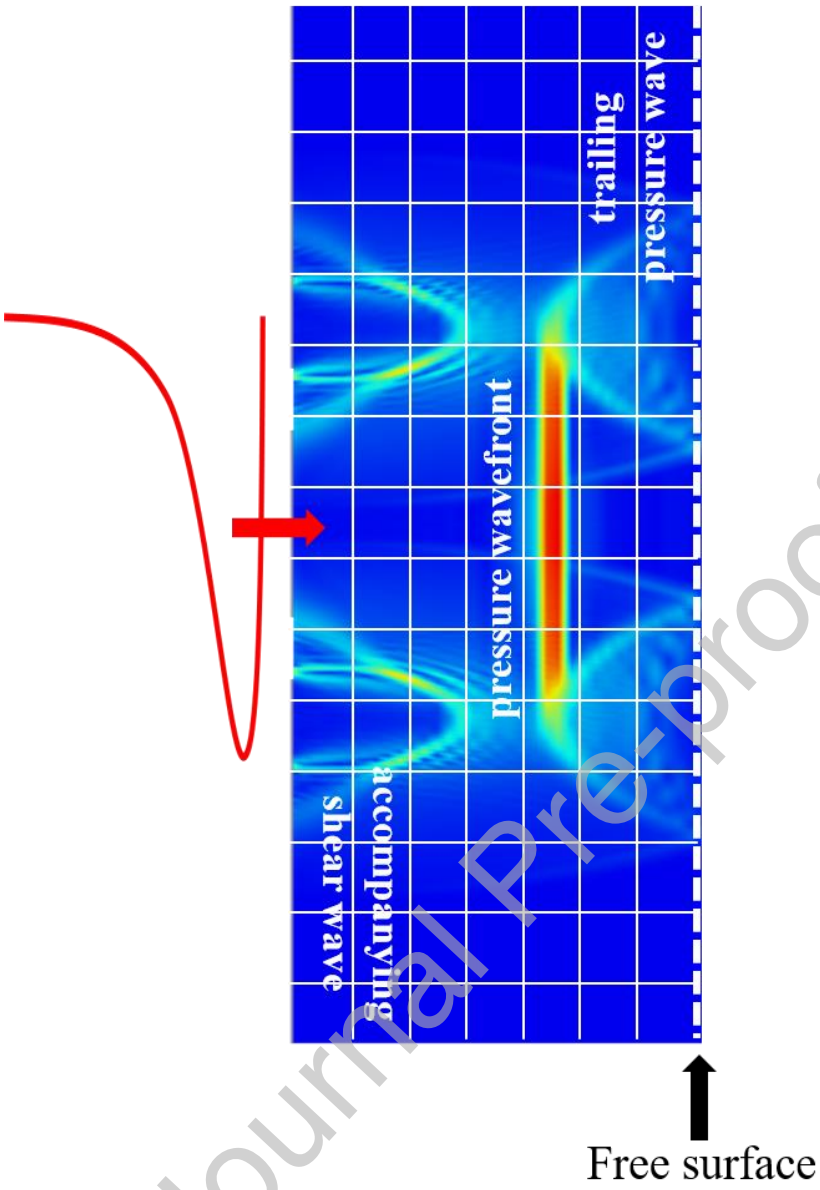

Abstract:

Computational studies can supplement existing ultrahigh strain rate experimental techniques in the absence of invasive full-field measurement and visualization. In this study, a computational model is employed to elucidate various phenomena accompanying the generation, propagation, and interaction of multimode shock waves in viscoelastic material. Specifically, a 4 mm diameter polyurea plug with a thickness of 0.5 mm was modeled as a linear viscoelastic solid, where the relaxation behavior of the shear modulus was described using a Prony series while the Bulk modulus was assumed to be linear elastic based on the Poisson's ratio of polyurea. The results are presented in three case studies, where a different type of shock wave was emphasized in each case while focusing on the regions at the leading and trailing edges of the shock wavefront. Generally, the wavefront interacted with the accompanying and reflected waves, resulting in

compromising the purity of the sought-after loading condition, especially during the return trip of the wave upon approaching the free surface. In Case Study I, the propagation of laser-induced pressure wave remained pure during the forward trip towards the free surface but was compromised by the accompanying shear wave and side spherical patterned pressure waves. Case Study II simulated the generation of surface waves by incorporating a ring-shaped loading site, where the release of a surface displacement was found to be focused and amplified at the central point. In the final case study, Case Study III, the applied shear wave at ultrahigh strain rate generated secondary pressure and horizontal shear waves at the edges of the loading site, which complicated the loading scenario but provided new insight into the interaction of laser-generated shock waves with the solid. The results can be used to improve the analysis of experimental data to quantify the accompanying deformation and failure mechanisms of polymers subjected to hypervelocity impacts.

Keywords: Polyurea, multimode shock waves, in-silico, ultra-high strain rate.

***Corresponding author:** gyoussef@sdsu.edu

1. Introduction

The continuous emergence of shock-tolerant and shock-resistant structures and materials requires rigorous methods to evaluate its structural and mechanical integrity in response to shock loading from hypervelocity projectiles. Several experimental methods have been used for decades to advance the state of knowledge but have some debilitating limitations, such as not reporting the full-field stress and strain states as a function of relatively short loading times. Recent experimental research pursued high-speed digital image correlation methods, with some reported and foreseen roadblocks in terms of the available frame grabbing capabilities related to the loading rate. Most shock loading material testing mechanisms are suitable for a single shock event, following an elaborate and expensive experimental setup preparation. After the single shock event, a prolonged downtime is needed to extract the tested structure and reload a new virgin sample for subsequent testing. In addition to these experimental methods, computational analyses have been either an integral or supplementary part of the shock testing methods. For example, in laser-induced shock waves, discussed in detail later, a two-dimensional finite element solution is sought in tandem with the experiment to explicate the stress at the corresponding depth of spallation. In some instances, e.g., purely elastic response of time-independent materials, the finite element simulation can be replaced by one-dimensional elastodynamic solutions, similar to what has been reported in [1–3]. This current study aims to accelerate the study of shock loading material by providing insight into the mechanical response at the leading and trailing edges of the shock wavefront using an in-silico approach. The shock event emphasized in this study replicates multimode stress waves based on laser-induced shock wave testing apparatus.

In-silico methods have significantly impacted several disciplines, including materials science and engineering and mechanical sciences [4]. Computer-based models can simulate how a material mechanically responds under different geometrical configurations and external stimuli over a broad range of temporal and spatial scales. However, only a representative finite element model that accurately captures the details of the problem at hand can reduce the amount of experimentation by simulating mechanical responses. In the past, computer-based models have been used to simulate nanosecond shock wave-induced surface acoustic waves [5], attenuation of shock waves in geometrically complicated metal plates [6], and propagation of seismic waves from earthquakes [7]. Zhang *et al.* experimentally and numerically studied the propagation of spherical laser-induced shock waves, leading to confirmation of the stress state corresponding to fracture failure [5]. They investigated a relatively low range of stress amplitudes (up to ~10 MPa) and rates (impulse pressure within the microsecond rise time range). Zhang *et al.* found that the direction of the principal stress in a circular pattern coincided with the trajectory of crack initiation, hypothesizing the utility of their finding in the generation of high loading rate applications, e.g., reducing the likelihood of a concussion [5]. Furthermore, they ascertained the utility of finite element simulations for identifying and visualizing the propagated shock waves at the boundary between the two adjacent media used in the study. Kumar *et al.* leveraged computational analysis to investigate the effectiveness of perforation and porosity in armor plates on mitigating the bluntness of shock events [6]. They simulated a shock tube condition up to 1.3 MPa at a Mach number ranging from 1.2 to 1.6. Kumar *et al.* concluded that the shock waves lose its momentum as well as the peak pressure as it passes through these attenuated, perforated plates, based on the results of the computational analysis, [6]. Moreover, computational analyses are effective in studying large-scale problems, including the propagation of seismic waves

surrounding vital infrastructures such as dams and bridges, which are otherwise prohibitively expensive to study [7].

A vital aspect of computational analyses is a well-defined constitutive behavior model of the material and representative boundary conditions congruent to those present during experimentation or field deployment. Materials behave differently depending on the strain rate, i.e., rate of deformation. When the strain rate is above 10^2 s^{-1}, it is considered a high strain rate, and the load is classified as dynamic. Generally, the strain rate regimes are $10^2 < \dot{\varepsilon} < 10^4$ s^{-1} for high strain rate, $10^4 < \dot{\varepsilon} < 10^6$ s^{-1} for very high strain rate, and $\dot{\varepsilon} > 10^6$ s^{-1} for ultrahigh strain rate [8,9]. The latter is used to investigate fundamental material attributes such as flow stress, wave propagation, and failure processes. Different experimental techniques are used to accomplish a specific strain rate regime. Plate impact [10], laser-induced particle impact test (LIPIT) [11], and laser-induced stress wave [12–16] techniques can load materials at ultrahigh strain rate, i.e., $\dot{\varepsilon} > 10^6$ s^{-1}. The laser-induced shock waves (LSW) rely on focusing a high-energy pulsed laser on an energy absorbent sacrificial layer. This layer absorbs the energy and undergoes rapid thermal expansion that launches a high amplitude shock wave into the test structure. The compressive stress wave travels through the sample and reflects due to an acoustic impedance mismatch at the interface between different materials or at the free surface. When the amplitude of the reflected tensile wave exceeds the tensile strength of the sample, debonding of adjacent layers or spalling occurs, respectively. By changing the planar substrate into a triangular prism and allowing the originally generated longitudinal wave to mode-convert into a shear wave, Wang *et al.* successfully extended laser spallation to mixed-mode and pure-shear loading [15]. The application of the LSW technique has been extended from the adhesion of blanket thin films [15–17] to patterned thin films [18,19] and adhesion between biological cells and inorganic substrates [20,21] as well as the interfacial strength of directly bonded wafers. Recently, laser-induced shock waves have been used in microstructural material characterization to study nucleation, propagation, coalescence, dislocation mobility, and annihilation [22,23]. Overall, the laser-induced shock wave technique is unique since the time for creep or post-loading annealing is negligible based on the ultrahigh strain loading and is limited to the elastic strain regime.

A prominent example of shock-tolerant and shock-resistant material is elastomeric polyurea, which has been afforded a great deal of research in the past two decades, leading to a culmination of significant advancements by Barsoum [24]. Polyurea is a thermoset elastomer synthesized by an amine and an isocyanate polymerization, resulting in a domain-segregated microstructure consisting of hard and soft segments [25]. The segregated microstructure has been credited for its superior properties, including moisture-, chemical-, and abrasion-resistant, large extensibility before tearing, and hyperelastic attributes [26]. Additionally, polyurea has been investigated under a wide range of temperatures, environmental conditions, and strain rates [27], prompting its integration as a protective coating in civilian and military applications [28]. Plate impact experiments have been performed to evaluate the dynamic properties by Mock *et al.* [29]. Roland *et al.* used a drop weight test to investigate the uniaxial tensile response of polyurea at intermediate strain rates (0.06–573 s^{-1}) [30]. Sarva *et al.* [31], Shim and Mohr [32] conducted uniaxial quasi-static and split-Hopkinson-pressure-bar (SHPB) compression studies on polyurea over a range of strain rates (10^{-3}–10^4 s^{-1}). Youssef *et al.* have studied the polymer at ultrahigh strain rate (10^6 s^{-1}) using laser-generated pressure stress waves, reporting the overall mechanical response and the dynamic mechanical strength of 93.1±5 MPa [3,33–36]. The latter was found to be in excellent agreement with the results of the plate impact experiment performed by Jiao *et al.*

[26]. Subsequently, Gamez *et al.* investigated the shear response of polyurea also using laser-induced shock waves [37]. The overarching outcome of these experimental studies substantiates the technical importance of polyurea and exposes a gap in understanding the interaction between single or multimode shock loadings and the bulk material.

This research study aims to establish a computational analysis framework to elucidate the interaction of multimode laser-induced shock waves while emphasizing the regions at the leading and trailing edges of the shock front. This aim motivated the pursuit to answer some fundamental questions, including:

1) What is the evolution of the wavefront (temporally and spatially) as a function of propagation direction while accounting for the viscoelastic response of the material?
2) What are the byproduct waves birthing from the initial stress wave, and how do they affect the purity of the initial wave?

The present study includes the time-dependence response of polyurea using linear viscoelasticity in response to pressure, shear, and surface waves at ultrahigh strain rates (with nanoscale rise time). The outcomes can be used to enhance the future analysis of experimental data and motivate new in-situ or in-operando characterization techniques to quantify the accompanying deformation and failure mechanisms.

Computational Model

Several researchers have previously documented the elastodynamic solution; however, there are two overarching shortcomings of the current state-of-the-art [1–3]. First, the integration of time-dependent and nonlinear material behaviors increases the computational expense of the solutions since they require coupled temporal and spatial discretization. Second, the results are usually visualized in a minimalist approach, leaving crucial details about the interaction of the propagating stress wave with the solid at the wavefront obscured. The latter has created a gap in the fundamental understanding of the evolution in stress as the wave advances through the solid. To remedy these shortcomings, a computational model based on the finite element method was established in COMSOL Multiphysics (version 5.4) as part of this research study, enabling concurrent temporal and spatial discretization, thus, resulting in ease of visualization of the propagating stress wave in time and space. The time-dependent analysis solves the equation of motion

$$\rho \frac{\partial \boldsymbol{u}}{\partial t^2} = \nabla \cdot S + \boldsymbol{F}_v \tag{1}$$

where ρ is the density, $\boldsymbol{u}$ is the displacement field, S is the second Piola-Kirchhoff stress tensor, and $\boldsymbol{F}_v$ is the volume force [38]. The model also uses the following constitutive relations

$$S = S_0 + S_{ext} + S_q + C : \epsilon_{el} \tag{2}$$

$$S_q = \sum_i 2G_i(\tau_i \dot{\epsilon}_i) \tag{3}$$

$$\tau_i \rightarrow a_T \tau_i \tag{4}$$

where S_0, S_{ext}, and $S_q$are the initial, external, and viscoelastic second Piola-Kirchhoff stress tensor, respectively, C is the elasticity tensor, ϵ_{el} is the elastic strain, G_i is the shear modulus, τ_i

is the relaxation time, and a_T is the shift function [38]. The variables G_i, τ_i, and a_T are discussed later.

The spatial dimensionality of the computational model was adjusted depending on the waveforms, e.g., pressure vs. shear waves. The reduced models are discussed in the corresponding case studies. In what follows, the common aspects of the computational model are delineated, including the material model, discretization schema, and the mathematical representation of the input waveforms.

As discussed in the introduction, polyurea is an elastomeric thermoset with time-dependent properties and a nonlinear response. However, laser-induced shock waves load the samples at small strains under ultrahigh strain rate conditions, suppressing the inelastic deformation mechanisms, e.g., creep and plasticity, where the failure is commonly reported in the elastic region since the material has insufficient time to fail otherwise. Such a loading scenario has a twofold implication. First, the strain is limited to small deformation in the linear region of the stress-strain regime. Second, the time-dependent response plays a crucial role in the behavior. In short, the response of polyurea (or polymeric materials in general) to laser-induced shock waves can be sufficiently described by linear viscoelasticity, as shown in the recent literature [19,34–36]. Moreover, it was confirmed that the Time-Temperature Superposition Principle is valid for polyurea even at the high strain rates congruent with those used in the present virtual experiments (>10^5 s^{-1}) [36], extending the thesis first advanced by Zhao *et al.* [39]. We adopt the same approach here, which is succinctly summarized next.

Polyurea was modeled as a linear viscoelastic solid with a density of 1071 $kg \cdot m^{-3}$, pressure wave speed of 1750 $m \cdot s^{-1}$, and shear wave speed of 415 $m \cdot s^{-1}$ [40]. The Poisson's ratio was taken to be 0.486 [3,34,36,39,41], marking polyurea as a nearly incompressible material. The latter implies that the entire relaxation behavior of polyurea can be captured by the shear modulus, while the volumetric deformation can be represented with linear elasticity, i.e., volumetric deformation is time independent. The Bulk modulus was then taken to be 4.54 GPa [33]. The shear relaxation modulus, *G*, of the polyurea was based on the quasi-statically derived master curve and implemented using the Prony series with constants identical to those provided in Knauss and Zhao [39]. The Prony representation of the shear modulus is

$$G(t) = G_0 \left[\alpha_\infty + \sum_{i=1}^{n} \alpha_i exp\left(-\frac{t}{\tau_i}\right)\right] \tag{5}$$

where, *G(t)* is the relaxation shear modulus as a function of the relative moduli

$$\alpha_\infty = \frac{G_\infty}{G_0}, \qquad \alpha_i = \frac{G_i}{G_0} \tag{6}$$

and

$$G_0 = G_\infty + \sum_{i=1}^{n} G_i \tag{7}$$

with G_i representing the stiffness of the spring in the i^{th} branch and τ_i is the corresponding relaxation time constant of the same spring-dashpot pair. G_∞ is the long term shear modulus or steady state stiffness, derived from the material properties [38]. The value of the relative moduli and their associated time constants are given in Table 1.

Table 1: Relative shear moduli and corresponding time constant (s) for polyurea.

	1	2	3	4	5	6	7	8	9
τ_i	10^{-13}	$5X10^{-13}$	10^{-12}	10^{-11}	10^{-10}	10^{-9}	10^{-8}	10^{-7}	10^{-6}
α_i	0.036	0.036	0.036	$4.09X10^{-17}$	0.222	0.176	0.116	0.092	0.063

	10	11	12	13	14	15	16	17	18
τ_i	10^{-5}	10^{-4}	10^{-3}	10^{-2}	10^{-1}	1	10	10^{2}	10^{3}
α_i	0.042	0.037	0.019	0.016	0.010	0.008	0.005	0.005	0.009

The data provided in Table 1 was based on a master curve with reference temperature of 0°C, since laser-induced shock wave experiment is commonly done at room temperature, hence the time-temperature shift factor (a_T) according to the WLF equation was used [33].

$$log(a_T) = \frac{-C_1(T-T_r)}{C_2+(T-T_r)} \tag{8}$$

Where, T is the test temperature (herein was taken to be room temperature), C_1=8.86 and C_2=101.6.

Generally, unless otherwise noted in each of the following case study, the finite element model was spatially discretized with a uniform mesh and an element size of 15 μm, which was chosen to avoid internal wave reflection artifacts known to arise from non-uniform meshing. The non-dimensional quantity of the Courant-Friedrichs-Levy condition was used to calculate the time step to satisfy the standard numerical stability requirements based on the relationship between the element size (Δx), the wave speed of polyurea (c), and the time step (Δt), such that

$$CFL = \frac{c\Delta t}{\Delta x}, \;\; CFL \leq 1 \tag{9}$$

resulting in a time step of 2 ns at the expected strain rate of 10^6 s^{-1} [34,42–44].

The attributes of the stress profile resulting from the interaction of the high-energy pulsed laser with the sacrificial layer depend on the characteristics of the laser itself (e.g., energy, rise time, pulse duration, and wavelength) as described by Lindl's equation [45,46]. However, during the physical experiment, the stress profile is determined based on an interferometrically-measured free surface displacement [34]. Given the long history of the laser-induced shock wave experiment, e.g., [47], an idealized stress wave profile was used based on the previous experimental reports by Gupta *et al.* [33], regardless of the loading mode. The idealized input stress wave profile (σ_i), shown in Figure 1, can be described by

$$\sigma_i = -\frac{\rho c}{2}\left\{\gamma\left[exp^{\left(-\frac{t}{\alpha}\right)} - exp^{\left(-\frac{t}{\beta}\right)}\right]\right\} \tag{10}$$

where, ρ is the density of the substrate and c is the speed of sound of the material, while α, β, and γ are fitting parameters determined based on the interferometric displacement data. Here,

γ=333 m·s^{-1}, α=16.5 ns, and β=6.7 ns were selected to generate the input wave shown in Figure 1.

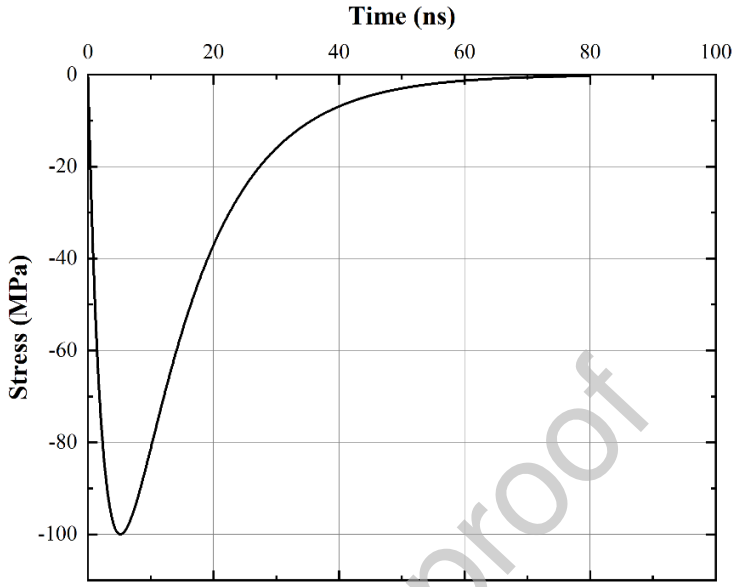

Figure 1: A general profile of the idealized input stress wave (Eqn. 10) with an amplitude of 100 MPa, rise time of 2.88 ns, and duration of 80 ns. This idealized profile is used as the input load due to laser-induced shock waves, simulating the propagation of pressure, surface, and shear waves independently.

Before embarking on the mechanical response of polyurea due to the propagation of different modes of stress waves, it is warranted to comment on the thermal effect due to the high-energy laser interaction with the sacrificial layer to create the stress wave. This is a common concern of novice investigators of this experimental protocol, given that the sacrificial layer undergoes rapid thermal expansion before exfoliating to launch the stress wave. Zhang *et al.* [48] recently performed a one-dimensional heat conduction analysis to elucidate the local increase in temperature in the sacrificial layer, and according to their results, the ablation layer surface can reach up to 5500 K. However, the poor thermal conductivity of polymers and the large time constant of the heat transfer process limit the effect of this increase in temperature to the surface of the test structure adjacent to the sacrificial layer.

Three case studies are reported below to explicate the separate and concurrent effect of pressure, shear, and surface waves on a 4 mm diameter plug of polyurea with a thickness of 0.5 mm. The first two case studies (propagation of pressure and surface waves, separately) employed a 2D axisymmetric model, where the corresponding boundary and loading conditions are shown in Figure 2. Two arbitrary points were fixed in all directions ($\boldsymbol{u} = 0$) to prevent rigid body motion during the simulation due to the imparting stress wave. The lateral sides of the polyurea plug were ascribed with low-reflecting boundary conditions to avoid reflection of the wave disturbance from these boundaries throughout the simulation; hence, the results discussed next are due to the propagation of the stress wave. The low-reflecting boundary condition tries to create a perfect acoustic impedance match by considering the material data from the adjacent domain so that

$$\boldsymbol{\sigma} \cdot n = -\rho c_p \left(\frac{\partial u}{\partial t} \cdot n\right) n - \rho c_s \left(\frac{\partial u}{\partial t} \cdot t\right) t \tag{11}$$

where, n and t are the unit normal and tangential vectors at the boundary, respectively, and c_p is the speed of the pressure wave while c_s is the speed of the shear wave [38]. For Case Study I, the input pressure wave was prescribed on the bottom surface (see Figure 2) using the stress wave profile shown in Figure 1 while the top surface was left traction-free. For the second Case Study (i.e., the propagation of surface waves), the stress wave was applied to the top surface in a ring-shaped spot while the bottom side was left traction-free in this scenario. The dimensions of the ring area are 800 µm in mean diameter and 100 µm thick.

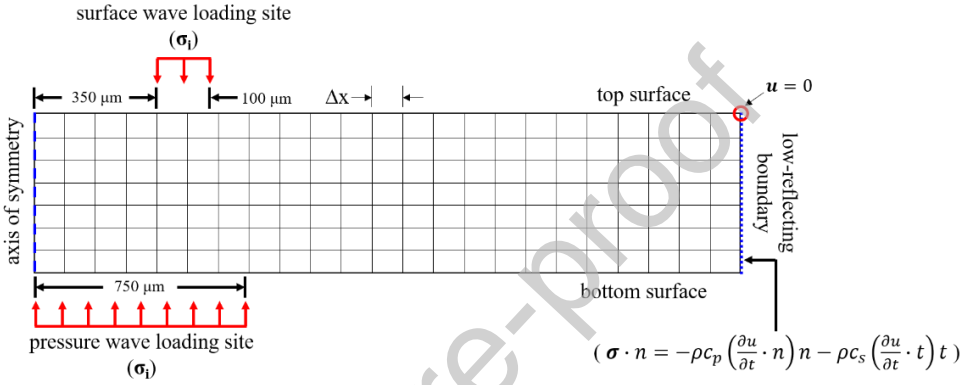

Figure 2: Schematic representation of the 2D axisymmetric model with the corresponding boundary conditions used in simulating the propagation of the pressure and surface waves in elastomeric polyurea due to laser-induced shock waves.

The final case study (propagation of shear waves) was performed using a 2D plane strain model. This modeling approach was taken due to the asymmetric propagation of the shear wave into the thickness of the simulated polyurea plug. The shear wave was applied at the bottom surface, with a spot size of 1.5 mm. The ratio of the loading site diameter to the thickness of the disc was consistent with previous studies [34]. The general details of the model and the material properties remain faithful to the description above, regardless of dimensionality or type of the propagating wave.

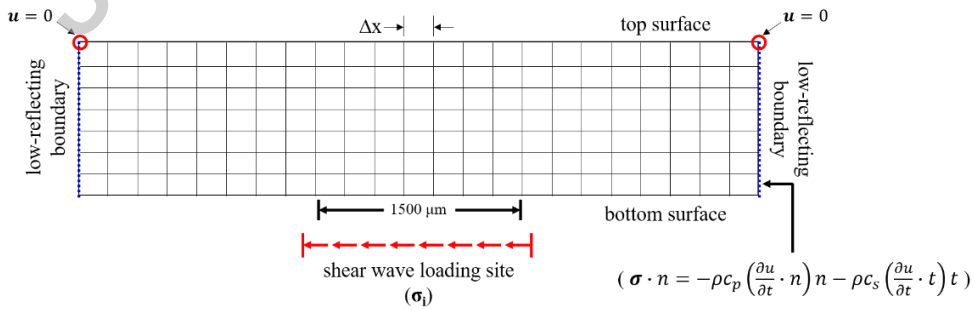

Figure 3: Schematic representation of the 2D model with the corresponding boundary conditions used in simulating the propagation of the shear waves in elastomeric polyurea.

The mapped mesh (displayed schematically in Figures 2 and 3) was selected to avoid nonlinear convergence behavior. A fully coupled iterative finite element solution with a fully coupled iterative solver was implemented while the displacement fields were calculated with the MUMPS linear system solver. Each successive solution step included an error estimate check to ensure solution convergence and accuracy.

Case Study I: ***Propagation of Pressure Waves***

Figure 4 is a composite figure of the contour plots of the effective stress at different simulation times, ranging from 0 ns to 600 ns, and the corresponding line plots of the normal stress component as a function of time at different locations along the propagation path. The extracted initial amplitude of the pressure stress wave was 138.04 MPa, arriving at the free surface in 291 ns, which is in good agreement with the prediction based on the wave speed. The free surface reflection is a tensile wave moving at the same speed, still exhibiting some of the characteristics of the original wave while plowing through the solid during the forward trip. While the width-at-half-maximum (FWHM) and rise time of the original wave were 8.06 ns and 4.35 ns, respectively, the same attributes of the reflected wave were found to be 22.94 ns and 13.97 ns. The FWHM, rise time, and the amplitude of the wave as a function of travel distance are plotted in Figure 5, where the reflection off the free surface occurred after 300 ns.

The line plot results (Figure 4) and the corresponding wave attributes seen in Figure 5 indicate that the initial ~130 ns of the wave propagation exhibited an asymmetric response analogous to the initial wave profile, shown in Figure 1 as a rapid rise and slow decay. The steady reduction in the amplitude is attributed to the material dispersive nature, also exemplified in the broadening of the wavefront in the accompanying contour plot. The narrow and sharp wavefront continues to widen as the wave propagates forward. This broadening effect is also exhibited in the reflected wave as it travels towards the bottom surface. As the wave crosses the ~130 ns temporal milestone, it experiences a conversion from an asymmetric to symmetric wave, as depicted in the wave profiles shown in Figure 4. The conversion is marked by a sudden change in the wave attributes, including the amplitude, rise time, and FWHM, as exhibited in Figure 5. Similar to the pre-conversion stage, the amplitude appears to decrease at nearly the same rate again due to the dispersive behavior of the material.

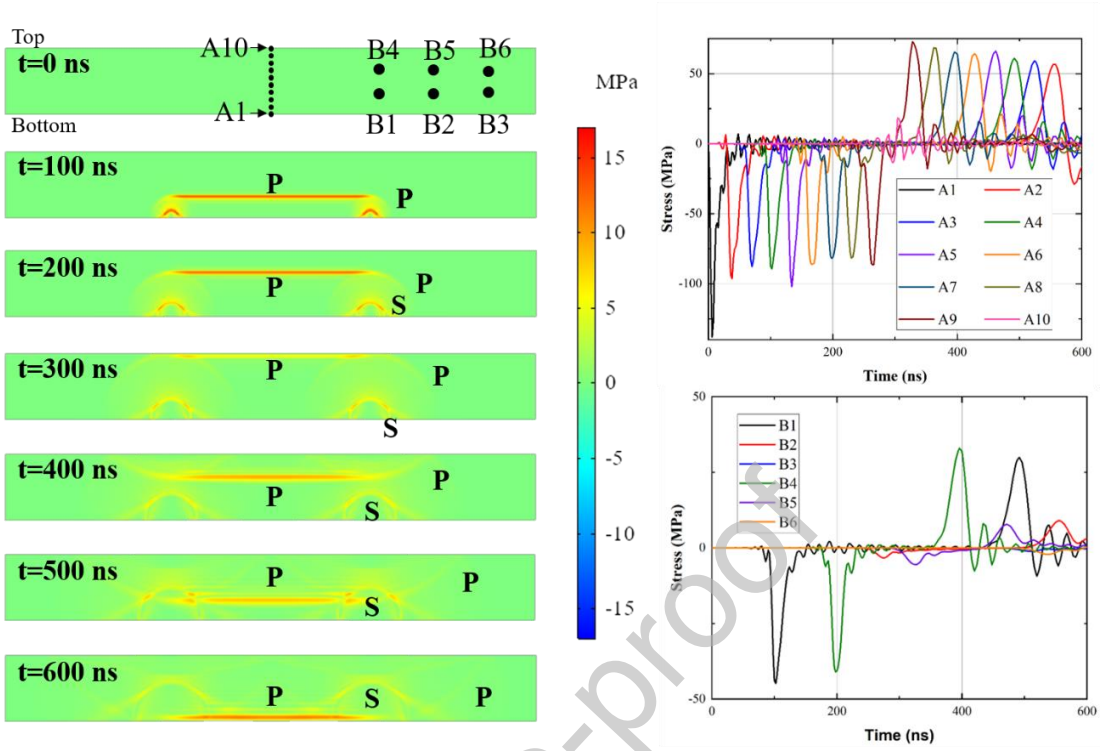

Figure 4: (left panel) contour plots of the effective stress due to the propagation of the pressure wave in elastomeric polyurea due to laser-induced shock waves, showing the flat pressure wavefront and the accompanying spherical wavefronts. (right panel) Line plots of the normal stresses extracted at different axial and lateral locations to demonstrate the dispersion and attenuation of the wave as it traverses the thickness of the plug.

The results in Figure 4 manifest two additional observations. First, the reflected wave, as expected, has a tensile sense after encountering the top free surface. This tensile wave loads the sample in a uniaxial state of stress, resulting in spallation if the amplitude exceeds the cohesion strength of the material. The amplitude of the reflected tensile wave in this case study was found to be 65.55 MPa, which is below the limit set before in [34] for the dynamic strength of polyurea. If such behavior is of interest, contrary to the objective of the current study, the amplitude of the input wave needs to increase, so the reflected tensile wave has enough momentum to fail the material catastrophically incrementally. It is worth noting that the cohesion limit is set experimentally by increasing the laser energy fluence while monitoring the free surface displacement interferometrically to deduce the input stress profile. Second, the contour plots show that the wavefront edges start to radiate away in spherical patterns at the same speed as the main wave. After a significantly delayed time, a trailing shear wave starts to nucleate at the edges of the original input location and radiates into the bulk of the solid in spherical patterns. The effect of the shear waves on the roundtrip of the pressure wave can be deduced from Figure 4, where the amplitude of the detected wave from the lateral direction is comparable to the wave originating from the interaction of the laser with the sacrificial layer. The spherical waves, at a propagation time between 400 ns and 500 ns, and the reflected tensile wave start to interact with the trailing shear waves, hence, loading this region of the sample multiaxially. The reflected tensile wave will first encounter its wake, or the trailing spherical waves originating

from the edges still carrying the original compressive sense. Such interaction results in interference that will modify the purity of the tensile wave and reduce its amplitude. Subsequently, the reflected tensile wave will encounter the shear waves with the spherical front that had started from the edges of the loading site.

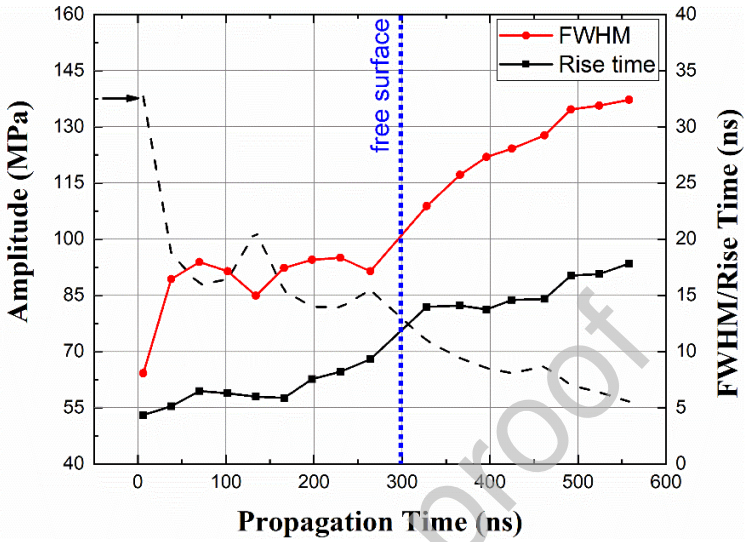

Figure 5: Wave attributes as a function of the propagation time of the pressure wave, including the amplitude in MPa, the full-width-at-half-maximum in ns, and the rise time in ns.

Case Study II: ***Propagation of Surface Waves***

Figure 6 presents a series of contour plots of the shear (left panel) and normal (right panel) stress components, extracted from the simulation of the propagation of surface waves up to 600 ns at 200 ns increments. Veysset *et al.* recently showed that the high energy laser spot could be reshaped into a ring, which upon the interaction with a blanket gold film, resulted in the propagation of surface waves along the free surface, causing failure at the center of the ring due to the focusing of the inwardly propagating surface waves [49]. Notably, the illumination of the laser on the metallic film also launches pressure and shear waves that travel into the bulk of the substrate towards the bottom surface. The slower shear wave can be seen (Figure 6a) propagating in the same direction as the initial pressure wave after ~100 ns in a spherical pattern. The pressure wave travels at a speed of 1750 $m \cdot s^{-1}$, while the shear wave moves at a slower speed of 415 $m \cdot s^{-1}$. The Rayleigh (c_R) surface wave speed is $c_R = c_s(0.87 + 1.12\nu)/(1 + \nu)$ or ~95% of the shear wave speed based on the Poisson's ratio listed in the previous section [50]. The interaction between the high-energy laser and the sacrificial layer results in a Rayleigh wave, and bulk pressure and shear waves.

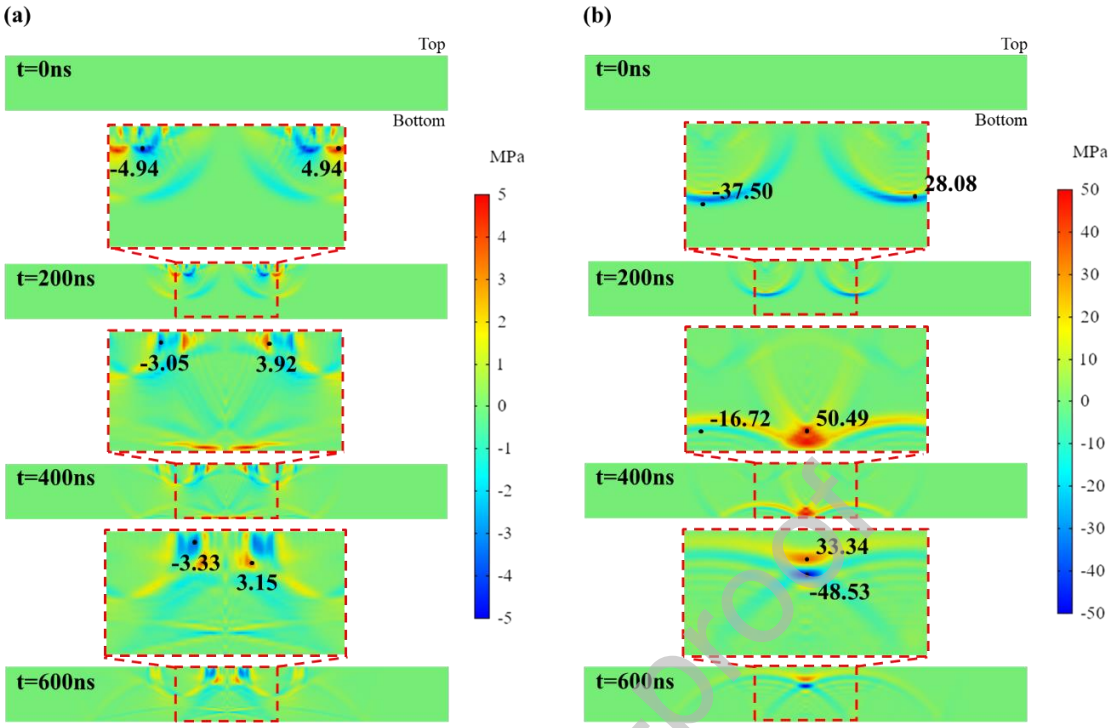

Figure 6: Contour plots of the (a) shear and (b) normal stress components due to the propagation of the surface wave (all listed stress numbers are in MPa) at different propagation times ranging from the onset of the simulation (top panel) to 600 ns (bottom panel). The central region at each simulation time is emphasized to better visualize the wave-to-wave interactions.

Two noteworthy observations can be discussed based on the contour plots in Figure 6. First is the propagation pattern of the Rayleigh waves. As seen from the 200 ns contour plot of Figure 6a, the shearing at the edges of the inner and outer diameter of the ring are initialized in the opposite directions. Over time, the waves develop into circular patterns that are entrapped on the surface, thus creating a propagation of Rayleigh waves radiating from the inner and outer diameters. The waves emanating from the inner diameter converge, where the surface wave stresses combine, creating a concentrated value at the center (site of interest, e.g., the experimental work of Veysset *et al.* [49]). The waves radiating from the outer diameter travel away from the center and towards the low-reflective boundaries, where the roundtrip of any remnant reflections is beyond the simulation time and is not of interest in the current study. It is worth noting that while emphasis was given to the waves sourcing from the inner and outer edges of the ring towards the center or the low-reflective boundaries, respectively, the waves also travel laterally in the other directions. Second is the pressure wave interactions (Figure 6b) with the shear waves (Figure 6a) propagating through the bulk of the material. In this case, the wave propagation scenario discussed in Case Study I is recovered since focusing the laser on the surface of the ring launches a compressive wave into the bulk underneath the illuminated surface, similar to the traditional loading scenario laser-induced shock wave experiment.

Here, the utility of the current computational study is illustrated for the future design of experiment studies through two unique loading conditions. If a pure surface loading is desirable due to the propagation of Rayleigh waves, one must set the mean diameter of the ring and the thickness of the plug symbiotically, where the mean diameter dictates the time required for the arrival of the Raleigh waves to the center (i.e., site of pure loading) while the thickness of the plug sufficiently delays the roundtrip of the pressure waves. On the other hand, a combined loading can also be guaranteed by strategically violating the abovementioned symbiotic relationship between the mean diameter and plug thickness. A secondary byproduct of the results presented in Figures 6a and b is the clear visualization of the interactions between the bulk waves. Contrary to Case Study I, the illumination of a ring-shaped geometry generates stress waves with a torus shape wavefront instead of a flat wave; thus, two areas of initial pressure wave propagations were created. The pressure waves originating from the loaded site start to interact with one another at ~300 ns, at which time the tensile wave at the axial center of the polyurea plug continues to travel towards the bottom free surface, reflecting as a compressive wave at the free surface. This reflected compressive wave traveling towards the top surface encounters the sequential shear wave, starting from the loading site at >400 ns. The rendezvous location may be of experimental interest since it is positioned within the bulk of the material while under the influence of a multiaxial loading scenario. The amplitude of the pressure wave can be amplified by concurrently combining the loading scenarios from Case Studies I and II, which can strategically be done by delaying the release of the pressure wave to coincide with the arrival surface wave. Example results of the latter are included in Appendix A.

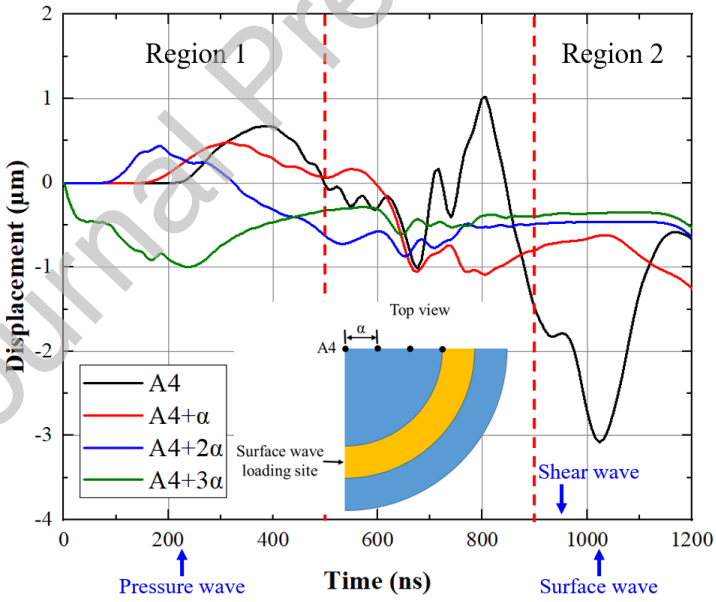

Figure 7: Displacement as a function of time at different locations on the top surface where α = 116.7 μm. The inset shows the location of the four points with respect to the laser-illuminated ring.

Figure 7 is a plot of the out-of-plane, normal displacement component corresponding to four points on the top surface (see inset in Figure 7) as a function of time. These four points were

selected to range between the inner diameter and the center of the laser-illuminated ring. The displacement-time history in Figure 7 can be divided into two regions, where region one covers up to 500 ns while region two extends beyond 900 ns. The compressive nature of the induced shock wave produces a negative displacement, i.e., a displacement into the bulk of the material at the inner rim of the ring, whereas the remaining points undergo a positive displacement due to volume conservation. With an emphasis on the displacement-time history of the point coinciding with the inner diameter of the ring (A4+3α point shown in the inset in Figure 7), the response starts to increase at a rate of 23 $m \cdot s^{-1}$ until it reaches a displacement of 0.45 μm within 20 ns, at which point it reaches a plateau that persists for ~60 ns. At the outset of the plateau region at 80 ns, the displacement commences to increase once more, but at a slower rate of 5 $m \cdot s^{-1}$. It is believed that the initial increase in the displacement at the beginning of the simulation time is attributed to the release of the pressure waves into the solid, while the subsequent increase is associated with the arrival of the accompanying shear waves. This observation can be substantiated by the temporal duration of the plateau, where the outset was fourfold of the inset and the rate of increase was maintained the same proportion, i.e., the same as the ratio between the pressure and shear wave speeds. The simulation was able to capture another behavior of the displacement-time history on the surface, which is the increase in the amplitude of the displacement as a function of the radial position. The increase in the amplitude is also accompanied by the peaks broadening, consistent with the response of the structure to plane waves due to an impulse loading and the focusing due to the convergence of the wave towards the center [51]. Similar to the response at point A4+3α, the onset of the peaks at the remaining points away from the inner diameter at 76 ns, 152 ns, and 216 ns, respectively, are due to the propagation of the pressure wave traveling at a speed of 1750 $m \cdot s^{-1}$. As previously noted, the Rayleigh surface wave travels at speed slower than the bulk waves (i.e., pressure and shear), ~394 $m.s^{-1}$; hence, the deformation observed at the region centered at 1050 ns corresponds to the propagation of the Rayleigh wave reaching the center of the loaded site.

Case Study III: ***Propagation of Shear Waves***

The contour plots in Figure 8 are based on the application of ultrahigh rate shear traction at the bottom surface (see Figure 3) with the characteristics of the idealized stress profile shown in Figure 1 and described by Equation 10. The release of the initial shear wave quickly evolves into three different wave types occupying the simulated plug: namely, a shear wave progressing vertically towards the top surface (S_V), another shear wave (S_H) orthogonal to the S_V wave moving towards the side boundaries, and a pressure wave (P) ahead of the S_V wave. The primary S_V wave and secondary S_H wave travel at the same shear wave speed, while the P wave moves faster. The latter can reverberate several times within the solid during the same time window the S_V wave makes a complete one-way trip towards the top surface. Hence, the reflected P wave interferes with the S_V wave first, followed by a subsequent interference with the S_H wave as it approaches the bottom surface. Since the P wave originates from the edges of the loading site, it propagates at only a fraction of the shear stress amplitude at 45° while developing into a spherical wavefront, as shown in Figure 8b. It is worth noting that the sense of the P wave is asymmetric about the central axis of the plug, where it has a positive tensile amplitude on the left (i.e., red color wavefront) and a negative compressive amplitude on the right (i.e., blue color wavefront) during the forward trip towards the top surface. Upon reflection from the free, top surface, the tensile and compressive waves interact (shown in the panel corresponding to t=600 ns in Figure 8b), resulting in interference patterns at 45° angle from the propagation direction,

which may develop in physical samples as shear bands. While the interference patterns are dramatized in the contour plots in Figure 8b (observe the denoted amplitudes at maximum red and blue areas), they appear to be inferior to the amplitude of the S_V and S_H waves. The shear stresses due to the propagation of the shear waves dominate the response. The more the P wave reverberates between the top and bottom surfaces and interacts with the shear waves, the less apparent its effects become due to the destructive nature of the interference.

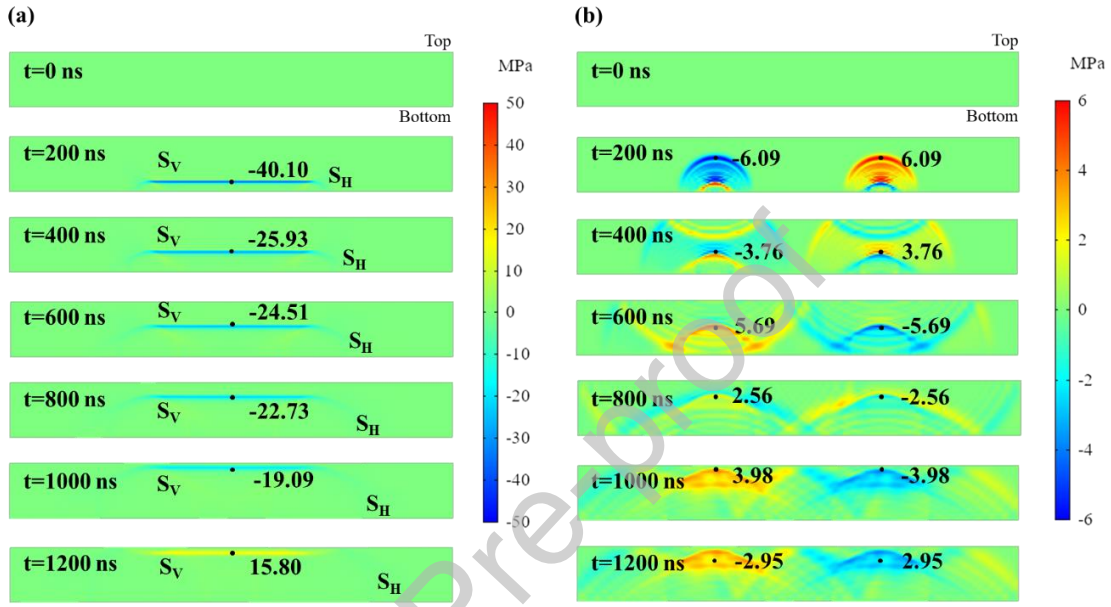

Figure 8: Contour plots of the (a) shear and (b) normal stress components as a result of the propagation of the shear wave, starting from the bottom surface, due to laser-induced shock waves with idealized profile described in Eqn. 10. The results are based on the model with the boundary conditions shown in Figure 3, where the stress numbers are in MPa.

Two final comments are warranted based on the contour plots in Figures 8a and b. First, the color alternations in the spherical propagation patterns of the P wave are associated with the areas in the sample under tensile stress adjacent to areas in compression (i.e., alternating blue and red regions along the wavefront). This alternation is evident at later simulation times upon the S_V wave interference, as the returning P wave is locally equilibrating the slowly propagating S_V wave. Second, the wavefront of the S_V wave appears to be broader than its counterpart from the pressure wave discussed in Case Study I, a result of the slow rate of propagation of the shear wave into the viscoelastic polyurea. As the shear wave plows through the thickness of the polyurea plug at a rate of 415 $m \cdot s^{-1}$, it activates additional and slower Prony elements that correspond to a compliant mechanical response, e.g., the relative shear modulus at a short-time Prony element is higher than a later and longer time element (see Table 1). In effect, the slow shearing rate extends the presence of the response and, in turn, broadens the peak. Such peak broadening can be clearly observed by comparing the FWHM values in Figure 9 based on analysis of the results from the current case study with those in Figure 5 from Case Study I. The FWHM of the shear waves slowly increased as a function of propagation time and axial location, changing from 14.96 ns for the initial wave to 67.64 ns in the shear wave approaching the top

surface. The peak broadening was also associated with a steady decrease in the amplitude, where it changed from 128.23 MPa for the input wave to 19.79 MPa for the wave near the top surface. The significant reduction in the amplitude over the 0.5 mm thickness is attributed to the quality factor of wave propagation in viscoelastic media, highlighting the impact mitigating properties of polyurea as reported in [33]. The destructive interferences between the fast and reverberating P wave and the S_V also reduces the amplitude.

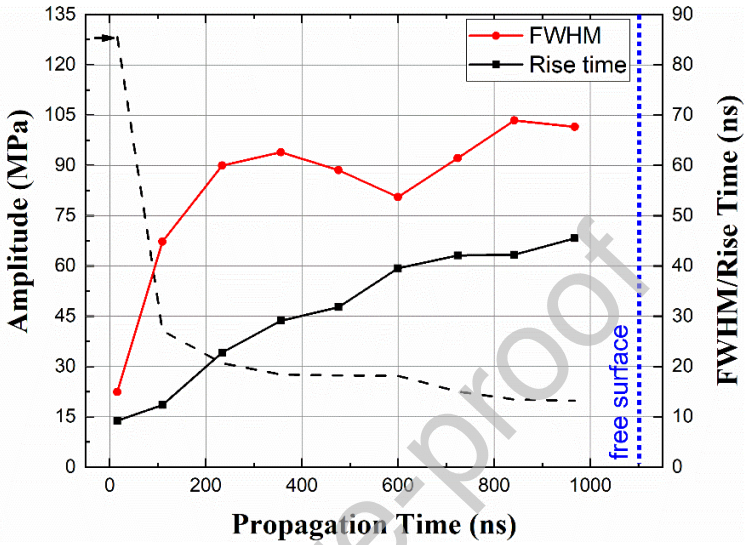

Figure 9: Wave attributes as a function of the propagation time of the shear wave, including the amplitude in MPa, the full-width-at-half-maximum in ns, and the rise time in ns.

Conclusion

A computational model was constructed and solved to explicate the full-field response of viscoelastic solid, e.g., polyurea, with laser-induced shock waves, emphasizing on the shock front. Three case studies were considered, elucidating the response of polyurea to pressure, shear, and surface waves when applied separately. The results indicate that the actual loading due to these ultrahigh strain waves is far more complicated than accurately captured by analytical elastodynamic solution. The results also provided an insight into the duration when the shock wave travels alone with a distinct wavefront and when the waves start interacting, leading to multimode loading, even if the objective was otherwise. Several strategies are discussed to tune the time of arrival of different wave types, which can be very beneficial to an experimentalist work in this area during the design process. Overall, the computational results demonstrated that the purity of the loading type would depend on the geometrical configuration and delay of concurrent input waves. Despite the application of a pure pressure, surface and shear wave, the interference of the accompanying waves alters the characteristics such as amplitude, pulse width, and rise time of the initial stress profile. In general, in-silico experimentation of multimode shock waves can be done prior to or in tandem with the physical experiment to determine parameters such as geometrical dimensions, loading type, etc., depending on the targeted failure mechanism or stress state.

Acknowledgement

The research was supported in part by the National Science Foundation, Award No. 1925539, and Department of Defense, Contract No. W911NF1810477. The authors are also grateful for internal funding from San Diego State University.

Author Statement

Carlos Gamez: Conceptualization, Visualization, Methodology, Investigation, Writing- Original draft preparation, Writing- Reviewing and Editing, Formal analysis. **Nha Uyen Huynh:** Data curation, Validation, Formal analysis, Writing- Reviewing and Editing. **George Youssef:** Conceptualization, Supervision, Writing- Original draft preparation, Formal analysis, Funding acquisition.

Declaration of interests

The authors declare that they have no known competing financial interests or personal relationships that could have appeared to influence the work reported in this paper.

References

[1] Mal AK, Banerjee S, Gupta V. Measurement of thin film interfacial properties using nanosecond laser source. Heal Monit Smart Nondestruct Eval Struct Biol Syst V 2006;6177:61770Y. https://doi.org/10.1117/12.660429.

[2] Youssef G, Moulet C, Goorsky MS, Gupta V. Inter-wafer bonding strength characterization by laser-induced shock waves. J Appl Phys 2012;111. https://doi.org/10.1063/1.4710987.

[3] Youssef G, Gupta V. Resonance in Polyurea-Based Multilayer Structures Subjected to Laser-Generated Stress Waves. Exp Mech 2013;53:145–54. https://doi.org/10.1007/s11340-012-9613-5.

[4] Mumy KL. Encyclopedia of Toxicology, 3rd Edition. London: Academic Press; 2014.

[5] Zhang Y, Yang C, Qiang H, Zhong P. Nanosecond shock wave-induced surface acoustic waves and dynamic fracture at fluid-solid boundaries. Phys Rev Res 2019;1:33068. https://doi.org/10.1103/PhysRevResearch.1.033068.

[6] Fan Y, Wang J. Attenuation of Shock Waves using Perforated Plates Attenuation of Shock Waves using Perforated Plates 2017. https://doi.org/10.1088/1757-899X/225/1/012059.

[7] Tadese BD. Finite Element Modeling of Seismic Wave Propagation in Earthen Embankments. University of Mississippi, 2012.

[8] Ramesh KT. High Rates and Impact Experiments. Springer Handb Exp Solid Mech 2008:929–60. https://doi.org/10.1007/978-0-387-30877-7_33.

[9] Field JE, Walley SM, Proud WG, Goldrein HT, Siviour CR. Review of experimental techniques for high rate deformation and shock studies. Int J Impact Eng 2004;30:725–75. https://doi.org/10.1016/j.ijimpeng.2004.03.005.

[10] Jiao T, Clifton RJ, Grunschel SE. High strain rate response of an elastomer. Shock Compression Condens Matter - 2005, Pts 1 2 2006;845:809–12.

[11] Sun Y, Kooi SE, Nelson KA, Hsieh AJ, Veysset D. Impact-induced glass-to-rubber transition of polyurea under high-velocity temperature-controlled microparticle impact. Appl Phys Lett 2020;117. https://doi.org/10.1063/5.0013081.

[12] Yuan J, Gupta V, Pronin A. Measurement of interface strength by the modified laser spallation technique. III. Experimental optimization of the stress pulse. J Appl Phys 1993;74:2405–10. https://doi.org/10.1063/1.354700.

[13] Pronin ANN, Gupta V. Measurement of thin film interface toughness by using laser-

generated stress pulses. J Mech Phys Solids 1998;46:389–410. https://doi.org/10.1016/S0022-5096(97)00081-1.
[14] Gupta V, Yuan J, Pronin A, Jun Y, Pronin A. Recent developments in the laser spallation technique to measure the interface strength and its relationship to interface toughness with applications to metal/ceramic, ceramic/ceramic and ceramic/polymer interfaces. J Adhes Sci Technol 1994;8:713–47. https://doi.org/10.1163/156856194X00447.
[15] Wang J, Weaver RL, Sottos NR. A parametric study of laser induced thin film spallation. Exp Mech 2002;42:74–83. https://doi.org/10.1007/bf02411054.
[16] Gupta V, Argon AS, Cornie JA, Parks DM. Measurement of interface strength by laser-pulse-induced spallation. Mater Sci Eng A 1990;126:105–17. https://doi.org/10.1016/0921-5093(90)90116-K.
[17] Vossen JL. Measurements of Film-Substrate Bond Strength By Laser Spallation. ASTM Spec Tech Publ 1978:122–33. https://doi.org/10.1520/stp38629s.
[18] Raman SN, Ngo T, Lu J, Mendis P. Experimental investigation on the tensile behavior of polyurea at high strain rates. Mater Des 2013;50:124–9. https://doi.org/10.1016/j.matdes.2013.02.063.
[19] Kim H, Citron J, Youssef G, Navarro A, Gupta V. Dynamic fracture energy of polyurea-bonded steel/E-glass composite joints. Mech Mater 2012;45:10–9. https://doi.org/10.1016/j.mechmat.2011.08.017.
[20] Hu L, Zhang X, Miller P, Ozkan M, Ozkan C, Wang J. Cell adhesion measurement by laser-induced stress waves. J Appl Phys 2006;100. https://doi.org/10.1063/1.2356107.
[21] Miller P, Hu L, Wang J. Finite element simulation of cell-substrate decohesion by laser-induced stress waves. J Mech Behav Biomed Mater 2010;3:268–77. https://doi.org/10.1016/j.jmbbm.2009.11.001.
[22] Youssef G, Crum R, Prikhodko S V., Seif D, Po G, Ghoniem N, et al. The influence of laser-induced nanosecond rise-time stress waves on the microstructure and surface chemical activity of single crystal Cu nanopillars. J Appl Phys 2013;113. https://doi.org/10.1063/1.4793646.
[23] Colorado HA, Navarro A, Prikhodko S V., Yang JM, Ghoniem N, Gupta V. Ultrahigh strain-rate bending of copper nanopillars with laser-generated shock waves. J Appl Phys 2013;114. https://doi.org/10.1063/1.4851055.
[24] Barsoum RGS, Dudt PJ. The fascinating behaviors of ordinary materials under dynamic conditions. Ammtiac Q 2010;4:11–4.
[25] Grujicic M, Yavari R, Snipes JS, Ramaswami S, Jiao T, Clifton RJ. Experimental and Computational Study of the Shearing Resistance of Polyurea at High Pressures and High Strain Rates. J Mater Eng Perform 2014;24:778–98. https://doi.org/10.1007/s11665-014-1316-x.
[26] Jiao T, Clifton RJ, Grunschel SE. Pressure-sensitivity and constitutive modeling of an elastomer at high strain rates. AIP Conf Proc 2009;1195:1229–32. https://doi.org/10.1063/1.3295026.
[27] Youssef G, Whitten I. Dynamic properties of ultraviolet-exposed polyurea. Mech Time-Dependent Mater 2017;21:351–63. https://doi.org/10.1007/s11043-016-9333-9.
[28] Youssef G, Reed N. Scalable Manufacturing Method of Property-Tailorable Polyurea Foam, 2017.
[29] Mock W, Bartyczak S, Lee G, Fedderly J, Jordan K. Dynamic properties of polyurea 1000. AIP Conf Proc 2009;1195:1241–4. https://doi.org/10.1063/1.3295029.

[30] Roland CM, Twigg JN, Vu Y, Mott PH. High strain rate mechanical behavior of polyurea. Polymer (Guildf) 2007;48:574–8. https://doi.org/10.1016/j.polymer.2006.11.051.
[31] Sarva SS, Deschanel S, Boyce MC, Chen W. Stress-strain behavior of a polyurea and a polyurethane from low to high strain rates. Polymer (Guildf) 2007;48:2208–13. https://doi.org/10.1016/j.polymer.2007.02.058.
[32] Shim J, Mohr D. Using split Hopkinson pressure bars to perform large strain compression tests on polyurea at low, intermediate and high strain rates. Int J Impact Eng 2009;36:1116–27. https://doi.org/10.1016/j.ijimpeng.2008.12.010.
[33] Youssef G. Dynamic Properties of Polyurea. University of California, Los Angeles, 2010.
[34] Youssef G, Gupta V. Dynamic tensile strength of polyurea. J Mater Res 2011;27:494–9. https://doi.org/10.1557/jmr.2011.405.
[35] Gupta V. Adhesive and ultrahigh strain rate properties of polyurea under tension, tension/shear, and pressure/shear loadings with applications to multilayer armors. Elastomeric Polym. with High Rate Sensit. Appl. Blast, Shock. Penetration Mech., 2015, p. 1–411. https://doi.org/10.1016/C2013-0-19258-6.
[36] Youssef G, Gupta V. Dynamic response of polyurea subjected to nanosecond rise-time stress waves. Mech Time-Dependent Mater 2012;16:317–28. https://doi.org/10.1007/s11043-011-9164-7.
[37] Gamez C. Failure mechanisms of polyurea under high strain-rate. University of California Los Angeles, 2017.
[38] COMSOL Multiphysics. COMSOL Documentation. Comsol Software 2014.
[39] Knauss WG, Zhao J. Improved relaxation time coverage in ramp-strain histories. Mech Time-Dependent Mater 2007;11:199–216. https://doi.org/10.1007/s11043-007-9035-4.
[40] Qiao J, Amirkhizi A V, Schaaf K, Nemat-nasser S, Wu G. Dynamic mechanical and ultrasonic properties of polyurea. Mech Mater 2011;43:598–607. https://doi.org/10.1016/j.mechmat.2011.06.012.
[41] Whitten I, Youssef G. The effect of ultraviolet radiation on ultrasonic properties of polyurea. Polym Degrad Stab 2016;123:88–93. https://doi.org/10.1016/j.polymdegradstab.2015.11.009.
[42] Stampfli R, Newacheck S, Youssef G. Fully-coupled Computational Modeling of the Dynamic Response of 1-3 Multiferroic Composite Structures. Int J Mech Sci 2021;191. https://doi.org/10.1016/j.ijmecsci.2020.106086.
[43] Massachusetts Institute of Technology. Stability of Finite Difference Methods. Numer Fluid Mech Lect Notes 2009:75–81.
[44] Kinsler LE, Frey AR, Bennett GS. Fundamentals of Acoustics. New York: Wiley; 1982.
[45] Ready JF. Effects due to absorption of laser radiation. J Appl Phys 1965;36:462–8. https://doi.org/10.1063/1.1714012.
[46] Ready J. Industrial applications of lasers. Second Edi. 1997.
[47] Gupta V, Argon AS, Parks DM, Cornie JA. Measurement of interface strength by a laser spallation technique. J Mech Phys Solids 1992;40:141–80. https://doi.org/10.1016/0022-5096(92)90296-E.
[48] Zhang Y, Zhang D, Wu J, He Z, Deng X. A thermal model for nanosecond pulsed laser ablation of aluminum. AIP Adv 2017;7. https://doi.org/10.1063/1.4995972.
[49] Veysset D, Maznev AA, Veres IA, Pezeril T, Kooi SE, Lomonosov AM, et al. Acoustical breakdown of materials by focusing of laser-generated Rayleigh surface waves. Appl Phys Lett 2017;111. https://doi.org/10.1063/1.4993586.

[50] Graff KF. Wave motion in elastic solids. New York: Dover Publications; 1975. https://doi.org/10.1016/0003-682x(77)90009-3.
[51] Medick MA. On classical plate theory and wave propagation. J Appl Mech 1961;28:223–8.

Appendix A: Propagation of Surface and Pressure Wave

For the surface and pressure wave case, the same boundary conditions of the 2D axisymmetric finite element model apply (see Figure 2). In addition to that, the stress wave that was applied to the bottom surface was delayed by 500 ns with respect to the stress wave applied on the top surface. The delay was introduced to ensure simultaneous arrival of the pressure and surface waves at the top surface. A composition of the contour plots of the effective stress at different simulation times and the corresponding line plot of the normal stress component as a function of time is shown in Figure A1.

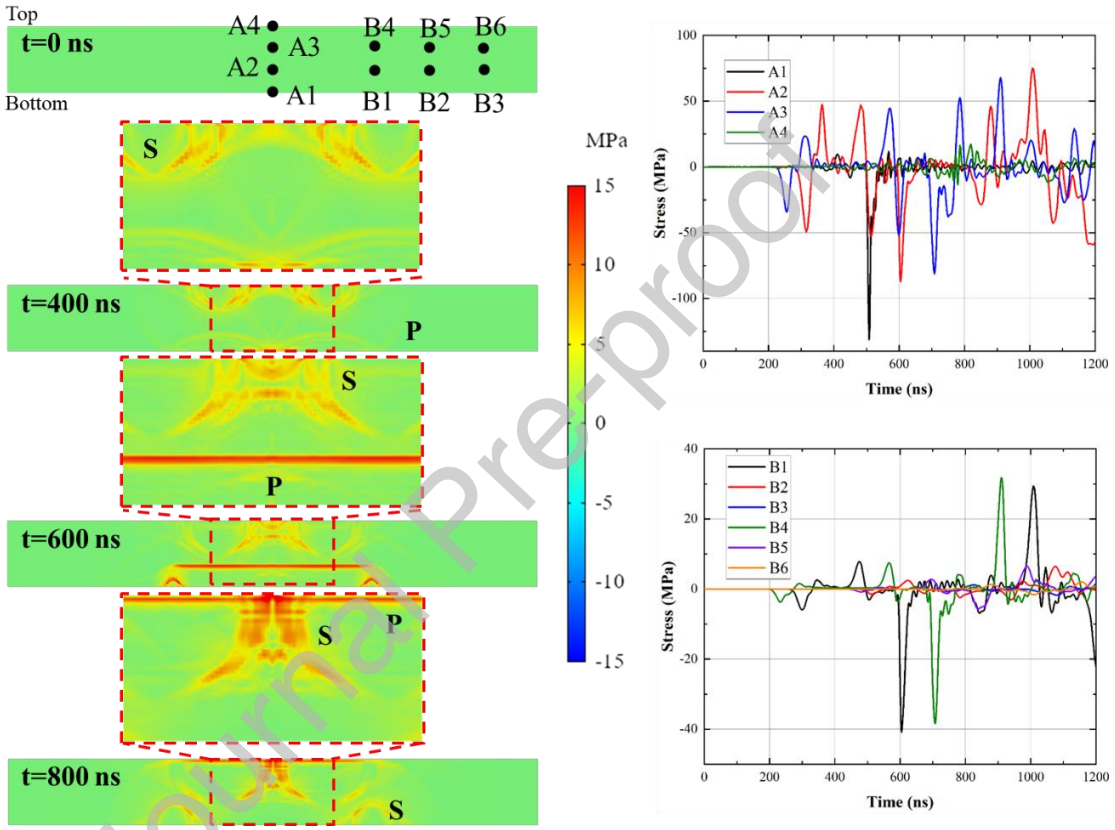

Figure A1: Concurrent propagation of the surface and pressure wave in elastomeric polyurea due to delayed release of pressure and surface waves to guarantee arrival at the site of interaction simultaneously. The loading and boundary conditions are shown in Figure 2.

Appendix B: Propagation of Pressure and Shear Wave

The propagation of pressure and shear waves were also studied, where the boundary conditions are shown in Figure 3. The stress wave was applied at the bottom of the plug while the release of the pressure wave at the same loading site was delayed by ~800 ns. Figure B1 is a composite figure of the contour plots of the effective stress at different simulation times, ranging from 0 ns to 1200 ns, and the corresponding line plot of the normal stress component as a function of time at different locations along the propagation path.

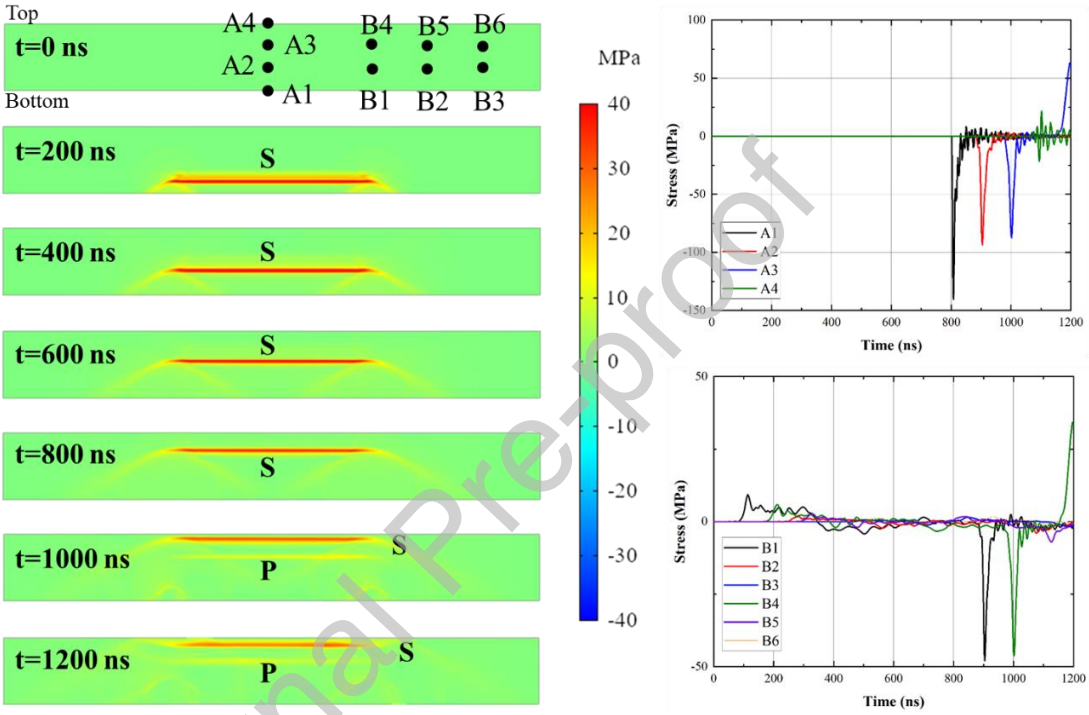

Figure B1: Concurrent propagation of the pressure and shear wave in elastomeric polyurea plug due to ultrahigh strain rate laser-induced shock waves based on the release of delayed pressure and shear waves to ensure simulations arrival at the top surface.